Journal of Materials Chemistry A

Accepted Manuscript

ROYAL SOCIETY OF CHEMISTRY

www.rsc.org/materialsA

Seed-assisted growth of α-Fe_2O_3 nanorod arrays on reduced graphene oxide: A superior anode for high-performance Li-ion and Na-ion batteries

Dezhi Kong,[a, b] Chuanwei Cheng,[a,*] Ye Wang,[b] Bo Liu,[b] Zhixiang Huang,[b] and Hui Ying Yang [b,*]

[a] *Shanghai Key Laboratory of Special Artificial Microstructure Materials and Technology, School of Physics Science and Engineering, Tongji University, Shanghai 200092, P. R. China. E-mail: cwcheng@tongji.edu.cn*

[b] *Pillar of Engineering Product Development, Singapore University of Technology and Design, 8 Somapah Road, Singapore 487372, Singapore. E-mail: yanghuiying@sutd.edu.sg*

Abstract

The α-Fe_2O_3 nanorods/reduced graphene oxide nanosheets composites (denoted as α-Fe_2O_3@r-GO NRAs) are fabricated by a facile and scalable seeds-assisted hydrothermal growth route, in which the α-Fe_2O_3 nanorods are assembled onto the side surfaces of r-GO nanosheets. Such α-Fe_2O_3@r-GO hybrid nanostructures are tested as anodes for both Li-ion and Na-ion batteries (LIBs and SIBs), which exhibits excellent performance with high capacity and long-cycling stability. When used for LIBs, the hybrid α-Fe_2O_3@r-GO NRAs electrode exhibits a highly stable Li^+ storage capacity of 1200 mAh g^{-1} after 500 cycles at 0.2 C and excellent rate capability. Moreover, the hybrid α-Fe_2O_3@r-GO NRAs also displays its versatility as an anode for SIBs, which delivers high reversible Na^+ storage capacity of 332 mAh g^{-1} at 0.2 C over 300 cycles with long-term cycling stability. The excellent electrochemical performance for the hybrid α-Fe_2O_3@r-GO NRAs anodes could be ascribed to the synergistic effect between the α-Fe_2O_3 nanorods arrays and reduced graphene oxide nanosheets, which could availably promote the charge transport and accommodate the volume change upon long-term charge-discharge process for reversible Li^+ or Na^+ storage.

Keywords: α-Fe_2O_3 nanorods, reduced graphene oxide, anodes, lithium-ion battery, sodium-ion batter

* To whom correspondence should be addressed: E-mail: [a] *cwcheng@tongji.edu.cn* or [b] *yanghuiying@sutd.edu.sg*

1. Introduction

The research and exploring of high-performance energy storage devices has gained great attention due to the increasing demand in portable electronic devices, electric vehicles as well as smart electric grids.[1-4] Rechargeable LIBs and SIBs are two types of most investigated storage devices due to their inherent advantages including high specific energy density, long lifespan and non-memory effect.[5-8] Especially, SIBs are particularly attractive in recent years as a potential alternative to LIBs, owing to the richin natural resources and low cost of sodium.[9,10] However, the size of Na^+ is larger than that of Li^+ (1.06 Å *vs.* 0.76 Å), making it difficult for sodium-ion fast inserted/extracted from the host materials.[11,12] In consideration of the above reasons, among various electrode materials for LIBs, only a few are suitable to accommodate sodium ions and allow reversible insertion-extraction reactions.[13-16] The development of suitable electrodes materials for both LIBs and SIBs with high capacity, long-term cycling life and high-rates capability is of great importance for high-performance energy storage devices.

Transition metal oxides (MO_x, M = Fe, Co, Mn, Ni, etc.) are widely investigated as anode materials for LIBs and SIBs due to their higher reversible specific capacities in contrast to that of carbonaceous anodes.[17-21] In particular, α-Fe_2O_3 with advantages of high theoretical capacity (~1007 mAh g^{-1}) and low cost is a promising candidate.[22-26] However, α-Fe_2O_3 usually suffers low conductivity and large volume expansion during the insertion/extraction processes of alkaline ion, result in poor cycling lifespan and low rates capability.[23,27] To addressing these drawbacks, one general strategy is to combine designed α-Fe_2O_3 nanostructures with carbon conducting matrixes such as thin-layer carbon shells, carbon nanotubes (CNT) and graphene or reduced graphene oxide (r-GO), forming hybrid composites to keep the structural integrity and improve the electrical conductivity of α-Fe_2O_3 based anode materials.[27-30] Especially, graphene with outstanding electrical conductivity, and excellent mechanical flexibility is an ideal conducting host for α-Fe_2O_3.[31,32] In the past few years, various Fe_2O_3/r-GO composites were fabricated and invesigated as anodes with improved performance. However, the Fe_2O_3 nanostructures like nanoparticles, nanorods and nanoplatelets are randomly anchored or adsorbed on the surfaces of r-GO nanosheets.[25, 33-34] Assembly of Fe_2O_3 nanorods on the sides surfaces of graphene nanosheets with ordered arrays structures would be more attractive to improve the electrochemical performance.[35] For instances, various nanostructured arrays assembled on reduces graphene nanosheets including PANI/r-GO NWAs[36], $ZnCo_2O_4$/r-GO NSAs[31],

TiO_2/r-GO NRAs[37] and $CoMn_2O_4$/r-GO NSAs[38] have been reported and demonstrated improved performance in LIBs.

Herein, we report a unique Fe_2O_3 nanorods/r-GO hybrid electrode structure design with 1D porous α-Fe_2O_3 nanorod arrays supported on both sides of 2D reduced graphene oxides nanosheets. This nanostructured electrode offers several advantages for energy storage in LIBs and SIBs. First, the 1D α-Fe_2O_3 nanorod arrays are directly grown on 2D r-GO nanosheets, which can prevent their restacking, as a result in improving the reversible capacity. Second, the r-GO network in the nanocomposites could facilitate the electron transportation and buffer the strain of α-Fe_2O_3 NRs, thus leading to improved cycling stability. Third, the α-Fe_2O_3@r-GO NRAs with porous characteristics and loose textures provide reduced resistance and short transportation pathway for ion diffusion and electron transfer, which would improve the rate capability. As expected, when tested them as anodes for both LIBs and SIBs, significantly improved electrochemical performance including high specific capacitance, good-rates capability and outstanding cycling stability are achieved in contrast to that of α-Fe_2O_3 and r-GO individual component, which are believed to be resulted from the 3D structural electrode design and the synergistic effect between the α-Fe_2O_3 nanorods and r-GO nanosheets.

2. Experimental Section

Synthesis of reduced graphene oxide (r-GO)

All of the reagents were of analytical grade and were directly used without further purification. Graphene oxide (GO) was synthesized from natural graphite flakes (> 99.8%, Alfa Aesar) according to the modified Hummer's method.[39] To fabricate the r-GO, the aqueous colloidal suspension of GO was prepared by ultrasonication of graphene oxide (135 mg) in de-ionized water (90 mL) for 2 h, followed by mild centrifugation (3500 rpm for 20 min) to remove thick layers. Afterward, the homogeneous GO colloidal suspension (90 mL) was placed in a 100 mL Teflon-lined autoclave, and treated by a hydrothermal process in a muffle furnace at 150 °C for 9 h, and then the black agglomerate sample was collected by centrifugation, and subjected to vacuum freeze-drying.

Synthesis of α-Fe_2O_3@r-GO nanorod arrays (α-Fe_2O_3@r-GO NRAs)

The α-Fe_2O_3@r-GO nanorod arrays were fabricated by a facile two-step seeds-assited hydrothermal growth process. In a typical procedure, 10 mg of r-GO was dispersed into 100 mL of deionized water by ultrasonication, and then 1.0 g of $Fe(NO_3)_3 \cdot 9H_2O$ was added. This mixture solution was slowly stirred for 2 h at 50 °C, then the precipitates were separated using centrifugation, washed several times with distilled water and ethanol, and

then vacuum freeze-dried. Next, 15 mg of the precipitate was dispersed in 35 mL of the solution containing of 0.432 g of $FeCl_3 \cdot 6H_2O$ and 0.864 g of $NaNO_3$ under stirring for 0.5 h. Then the resulting mixture was transferred into a Teflon-lined stainless steel autoclave and was hydrothermally treated for 12 h at 60 °C. After cooling down to room temperature, the precipitates were separated by centrifugation and washed with DI water several times, and then subjected to vacuum freeze-drying. Finally, the as-obtained samples were thermally annealed at 450 °C in Ar for 2 h to get crystallized α-Fe_2O_3@r-GO NRAs. For comparison, the pure α-Fe_2O_3 nanorods (α-Fe_2O_3 NRs) were also prepared in the same conditions in the absence of r-GO.

Characterization

The crystal structure of the products was analyzed by X-ray powder diffraction (XRD) using a Bruker D8 Advanced X-ray diffractometer with Ni filtered CuKa radiation (λ = 1.5406 Å, 40 kV, and 40 mA). The morphology, size, and chemical composition of the samples were characterized by field-emission scanning electron microscope (FESEM, JSM-6700F, JEOL Inc., Japan) equipped with an energy dispersive X-ray spectrometry (EDS), and the structures of the samples were executed by transmission electron microscopy (TEM, JEM-2100F, JEOL Inc., Japan). Raman spectroscopy were recorded at room temperature using a WITEC CRM200 Raman system equipped with a 532 nm laser source and 100× objective lens. The carbon content of the as-prepared samples was obtained by using a TG-DSC analyzer (Seiko Exstar 6000) under an air atmosphere in the temperature range of 20 to 1000 °C, and the heating rate was 5 °C min^{-1}. Specific surface area analysis was measured by N_2 adsorption-desorption isotherms at 77 K using the Brunauer-Emmett-Teller (BET, ASAP 2420, Micromeritics) method.

Battery Fabrication and Electrochemical Measurements

The electrochemical tests were analyzed using CR2032 coin-type cells at room temperature. The anodes of Li-ion and Na-ion batteries were prepared by mixing the active material, conductive carbon black, and polyvinylidene fluoride (PVDF) with a weight ratio of 80: 10: 10 in *N*-methyl-2-pyrrolidone (NMP) solution to form a slurry. The obtained slurry was uniformly pasted onto a Cu foil by a doctor blade and dried at 120 ℃ for 12 h in vacuum to remove the solvent, and then the electrode foil were punched into disks and pressed. For lithium-ion battery fabrication, the Li-metal circular foil as the counter-electrode, 1 M solution of $LiPF_6$ in ethylene carbonate (EC) and diethyl carbonate (DEC) (1:1 in volume) as the electrolyte, and a microporous polypropylene membrane (Cellgard 2400) as the separator. For sodium-ion battery fabrication, the metallic sodium foil as the counter-

electrode, 1 M solution of $NaPF_6$ in ethylene carbonate (EC)-diethyl carbonate (DEC)-fluoroethylene carbonate (FEC) (1:1:0.05 in volume) as the electrolyte, and glass fiber as the separator. The cells were assembled in an Ar-filled glovebox with moisture and oxygen concentrations below 0.1 ppm. Before testing, the cells should be aged for 15 h for ensure fully percolation of the electrolyte to the electrodes. The cyclic voltammetry (CV) and electrochemical impedance spectroscopy (EIS) tests were obtained using the same multichannel electrochemical workstation (*VMP3, Bio-Logic*, France). The galvanostatic charge/discharge cycling performance was performed in the voltage range of 0.01-3.0 V at various current densities from 0.1 C to 1.6 C (1C≈1000 mA g^{-1}) using a Neware (Shenzhen, China) battery-testing system.

3. Results and Discussion

The fabrication procedure of the α-Fe_2O_3@r-GO NRAs composite is illustrated in Fig. 1. The whole synthetic process involves four steps as follows: i.e., First, graphene oxide (GO) is prepared according to a modified Hummers route; Second, the GO is reduced to reduced graphene oxide (r-GO) through a simple hydrothermal process; Third, the as-obtained r-GO was then dispersed into an aqueous solution of $Fe(NO_3)_3$, after a low temperature reaction (50°C, hydrolysis reaction: $Fe^{3+}+3H_2O \rightarrow Fe(OH)_3 +3H^+$), the Fe-precursor nanocrystals-seeds are formed on the r-GO surfaces through the electrostatic forces. Finally, the α-Fe_2O_3 NRs were grown on both side surfaces of the r-GO nanosheets via a hydrothermal growth process, freeze-drying, and thermal treatment. The photographs of GO, r-GO, Fe-precursor@r-GO NPs and α-Fe_2O_3@r-GO NRAs dispersed in water were also displayed in inset of Fig. 1. As can be seen, the GO (sample I) could be well dispersed in water to form a stable yellow-brown dispersion because of the presence of large numbers of hydrophilic functionalized units on the nanosheets. However, when the GO was reduced in boiling water, the resulting black r-GO (sample II) floc dispersions are formed owing to the decrease of functional groups on the surface of the nanosheets. When the formation of the Fe-precursor seeds, almost all Fe-precursor@r-GO NPs (sample III) self-assembled and left an upper part transparent solution. After the α-Fe_2O_3 nanorod arrays grown, the α-Fe_2O_3@r-GO NRAs composite (sample IV) aggregates were precipitated to the bottom of clear solution, indicating that the hydrophobicity of the nanocomposite surface and complete electrostatic self-assembly between α-Fe_2O_3 NRs and r-GO nanosheets.

As shown in Fig. 2a, the SEM image of α-Fe_2O_3 nanorods exhibit uniform rod-shaped structures, with lengths of around 400 nm and diameters of around 80 nm. Fig. 2b shows the SEM images of an interconnected and porous framework with random open pores

constructed from r-GO nanosheets. The graphene-like nanosheets can be clearly observed in high-magnification SEM image (inset of Fig. 2b). The low-magnification SEM images in Fig. 2c and Fig. S1a show a frizzy morphology, consisting of an ultrathin wrinkled "paper-like" film structure. The high-magnification SEM images (inset of Fig. 2d and Fig. S1b), imply that amorphous Fe-precursor nanoparticles (NPs) are uniformly distributed on both sides of the r-GO nanosheets. The sizes of the Fe-precursor NPs are 2~6 nm, which can be further verified by the TEM images in Fig. S1c and 1d. The EDS spectroscopy and Raman spectra of the composites are provided in Supporting Information (See SI Fig. S2a-d). After the α-Fe_2O_3 growth, one layer of ordered α-Fe_2O_3 nanorod arrays were covered on both sides of r-GO nanosheets (as shown in Fig. 2e and 2f), demonstrating the strong coupling effect between α-Fe_2O_3 nanorods and the r-GO surfaces. The high-magnification SEM image in inset of Fig. 2f indicates the porous α-Fe_2O_3 nanorod arrays with a length of ~200 nm are interconnected with each other but not completely covering the whole r-GO nanosheets surfaces, which can keep a highly porous configuration and efficiently prevent the aggregation of r-GO nanosheets.

To further characterize the micro-structure of the α-Fe_2O_3@r-GO NRAs, TEM observations are conducted. For comparison, the TEM images of the pure α-Fe_2O_3 NRs and the r-GO sheets are also provided. For pure α-Fe_2O_3 NRs, uniform rod shape is clearly observed in Fig. 3a. From the HRTEM image in Fig. 3b, two sets of clear lattice fringes with the same interplanar distance of 0.25 nm are in good agreement with the spacing of the (110) and (-120) plane of α-Fe_2O_3.[34] The selected-area electron diffraction (SAED) patterns of pristine α-Fe_2O_3 (Fig. 3b inset) indicates its single-crystalline feature. Fig. 3c shows that the r-GO layers are almost transparent with some wrinkles visible under TEM. High-resolution TEM and SAED patterns (Fig. 3d) further indicate high-quality crystalline nature of r-GO nanosheets. For the composite materials (Fig. 3e), a sheet-like shape of graphene is uniformly deposited with numerous nanorods, and these rod-like α-Fe_2O_3 arrays are ~200 nm in length and about 30 nm in diameter at the middle section. The HRTEM image shown in Fig. 3f exhibits the lattice spacings of 0.23 nm and 0.25 nm correspond to the (006) and (110) planes of α-Fe_2O_3, respectively, indicating that each principal nanorod is a [001] oriented α-Fe_2O_3 single crystal.[34,40] The clear reflection spots in SAED pattern of Fig. 3e recorded from the in Fig. 3b can be indexed to the α-Fe_2O_3 crystal structure (JCPDS no. 33-0664).[30] The different crystal orientation of HRTEM images would be due to the morphology difference of α-Fe_2O_3 nanorods, as observed in Fig. 2a and f.

The surface electronic states and chemical compositions of the α-Fe_2O_3@r-GO NRAs composites are checked using X-ray photoelectron spectroscopy (XPS) (as shown in Fig.

S3). In the high-resolution XPS spectra of Fe 2p (Fig. S3b), two major peaks with binding energies at 710.2 and 724.6 eV are observed, assigning to the Fe $2p_{3/2}$ and Fe $2p_{1/2}$ level, respectively, are characteristic of Fe^{3+} species in α-Fe_2O_3.[41-43] The deconvolution peaks (Fig. S3c) of the O 1s spectrum are decomposed into four components using peak fitting, which are centered on 530.2, 530.8, 531.9 and 533.4 eV. One peak centered at 530.2 eV is attributed to the O^{2-} forming oxides with Fe, while the others can be ascribed to the C–O, O=C and C–OH/C–O–C in r-GO, respectively.[44] From the typical C 1s spectrum in the composites (Fig. S3d), four components are also seen at 284.6, 285.1, 286.4, and 288.9 eV, which are correspond to the C–C, C–O (epoxy and alkoxy), C=O (carbonyl), and O–C=O (carboxyl) bonds of r-GO, respectively.[44, 45]

The XRD patterns of the pure r-GO, α-Fe_2O_3 NRs, and the resulting composite of the α-Fe_2O_3@r-GO NRAs are shown in Fig. 4a. The patterns of pure α-Fe_2O_3 NRs shows clearly sharp peaks indexed to the hematite Fe_2O_3 (JCPDS no. 33-0664).[46] On the other hand, the pure r-GO shows a very broad diffraction peak at $2\theta \approx 25.0^{o}$, which means that all of the GO have been transformed to r-GO with significantly less functionalities.[47] After α-Fe_2O_3 decoration, the obvious diffraction peaks of r-GO and α-Fe_2O_3 can be observed, and all diffraction peaks match well with those of the hematite. No other impurities were found. Fig. 4b shows the Raman spectrum of r-GO, pure α-Fe_2O_3 NRs and α-Fe_2O_3@r-GO NRAs composite, respectively. The Raman spectrum of r-GO sample shows three characteristic peaks of graphene allowed lines at 1350, 1581 and 2722 cm^{-1}, which are in good correspond to the D, G and 2D bands, respectively. Moreover, the fundamental Raman scattering peaks for α-Fe_2O_3 are observed at 218, 277, 389, 486, and 595cm^{-1} corresponding to the A_{g1}, E_{g2}+E_{g3}, E_{g4}, A_{1g}, and E_{g5} modes, respectively.[48] All the characteristic bands of pristine α-Fe_2O_3 in the lower wave number range and the characteristic D and G bands of r-GO are also appeared clearly in the Raman spectrum of α-Fe_2O_3@r-GO NRAs, illustrating again the successful formation of the nanocomposite. A broad band at 1306 cm^{-1} in the spectrum of the pristine α-Fe_2O_3 does not appear in the α-Fe_2O_3@r-GO NRAs spectrum might be due to the overlapping with the strong D band (1350 cm^{-1}).

To further determine the constitution of the α-Fe_2O_3@r-GO NRAs, the EDS spectrum was performed. The presence of elements Fe, O, and C confirms the formation of α-Fe_2O_3 with r-GO, which is consistent with the XPS analysis. Fig. 5a shows the EDS elemental mapping of an area of the composites with uniform Fe, O, and C dispersion, which further confirms that the α-Fe_2O_3 NRs are homogeneously distributed on r-GO nanosheets. The EDS spectrum result shown in inset of Fig. 5a is in agreement with the SEM elemental mapping and further verifies the uniform presence of C, O and Fe (with a Fe/O molar ratio

of ~1.5). Moreover, the EDS analysis of the r-GO, pristine α-Fe_2O_3 NRs and the composite of α-Fe_2O_3@r-GO NRAs are also depicted in Fig. 5b. In both the pristine α-Fe_2O_3 and the composite α-Fe_2O_3@r-GO sample, the presence of Fe and O can be clearly found, and in both the r-GO and the composite α-Fe_2O_3@r-GO sample, carbon ("C") is present. These results corroborate the formation of the α-Fe_2O_3@r-GO composite. For reference, the EDS spectrum of pure α-Fe_2O_3 NRs and r-GO were also prepared, as shown in Fig. S4a-d. Fig. 5c shows the thermal behavior of the α-Fe_2O_3, r-GO and α-Fe_2O_3@r-GO NRAs, respectively. From the TGA curves, r-GO sample burns out at ~700 °C, while the pure α-Fe_2O_3 sample remains steady over the whole temperature range. For the α-Fe_2O_3@r-GO NRAs, the weight loss between 25-100 °C and 450-600 °C is attributed to the loss of absorbed water and the pyrolysis of r-GO, respectively. According to the change of weight, it is estimated that the mass percentage of r-GO in the α-Fe_2O_3@r-GO NRAs is ~17 %.

The nitrogen adsorption and desorption isotherms of the as-prepared r-GO nanosheets and α-Fe_2O_3@r-GO NRAs exhibit prominent characteristic of type IV (Fig. 5d), which are indicative of the presence of relatively large pores in the as-prepared samples. For pure α-Fe_2O_3 sample, a small step of the N_2 adsorption-desorption branches appears at the high relative pressure (P/P_0), due to the voids among these nanoparticles. It is worth noting that the Brunauer-Emmett-Teller (BET) specific surface area of the α-Fe_2O_3@r-GO NRAs composite (203 m^3 g^{-1}) is higher than those of pure r-GO (139 m^3 g^{-1}) and pure α-Fe_2O_3 powder (34 m^3 g^{-1}), which strongly suggests that the α-Fe_2O_3 NRs anchored on the separated r-GO surface prevent the r-GO nanosheets from aggregating and restacking, as illustrated in Fig. 2. The large specific surface area is beneficial to reduce the ion diffusion paths and enhance the utilization of active materials, as a result in improving electrochemical performance. Additionally, the pore size distribution of the samples is calculated using Barret-Joyner-Halenda (BJH) method as shown in inset of Fig. 5d. The as-prepared r-GO and α-Fe_2O_3@r-GO NRAs have similar pore-size distributions, from micropores to macropores. Importantly, the total pore volume of the α-Fe_2O_3@r-GO NRAs (0.426 m^3 g^{-1}) is higher than the pure r-GO sheets (0.360 m^3 g^{-1}), further indicating the separation of r-GO nanosheets induced by the loading of α-Fe_2O_3 NRs. For comparison, pore volume of pure α-Fe_2O_3 NRs is only 0.108 cm^3 g^{-1}, which confirms the dispersion interaction of r-GO sheets with α-Fe_2O_3 NRs.

In order to study effect of Fe^{3+} concentration on the morphologies of the as-prepared products, control experiments were carried out at different concentrations of $FeCl_3$ (0, 0.4, 0.8, 1.2, 1.6 and 2.0 mmol). From the SEM images of the *α*-Fe_2O_3@r-GO hybrids prepared with various amounts of $FeCl_3$ during the second hydrothermal process in Fig. 6a-e, we

found that the morphologies of α-Fe_2O_3 arrays are constantly vary with the Fe^{3+} concentration increasing from 0.4 to 2.0 mmol, and from the initial flake-like arrays are gradually transformed into rod-like arrays, even rod/flower-like arrays. The more detailed information is provided in Supporting Information. Noting that all the α-Fe_2O_3@r-GO nanostructures prepared with different $FeCl_3$ amount are evidenced in the orthogonal phase by XRD patterns (Fig. S5). Obviously, the Fe^{3+} concentration is crucial to control the nucleation, growth and morphology of α-Fe_2O_3@r-GO nanocomposites via the possible coordination effect between Fe^{3+} and $NaNO_3$. Noting that the $NaNO_3$ was employed as a structure-directing agent to facilitate the relatively uniform growth of 1D nanorods.[49] Without Fe^{3+} in the reaction system, the morphology is still unchanged, as shown in Fig. S6a, whereas there are small amounts of α-Fe_2O_3 nanorods irregularly deposited on the graphene without the Fe-precursor seeds, as shown in Fig. S6b. Thus, in the experimental system, there are two possible nucleation sites, i.e., bulk solution and graphene substrates, for the growth of α-Fe_2O_3 nanorods. These two sites compete with each other, the α-Fe_2O_3 nanorods are preferentially grown on the surfaces of the r-GO sheets, due to the Fe-precursor seeds presented in the surfaces of the r-GO sheets could furtherance the interfacial reaction between the solid surface and bulk solution.[50] Thus, the morphology of the resultant α-Fe_2O_3@r-GO hybrid structures can be adjusted by simply controlling the added amount of Fe^{3+} in the reaction solution. Moreover, to further explore the growth mechanism, the evolution of morphology and structure with varied times were studied at 60□ after 0, 3, 6, 9, 12 and 15 h and after heat treatment at 450□ for 2 h in air. The detailed results are revealed in Fig. S7.

The electrochemical performances of as-prepared samples were explored by testing them as anodes for LIBs. The relationship between the morphology structure and lithium storage property is first discussed. Fig. S8a-d and Fig. 7a illustrate a comparison on the first five galvanostatic charge-discharge profiles of the different α-Fe_2O_3@r-GO hybrid electrodes that prepared under various amounts of $FeCl_3$ during the second hydrothermal process, respectively, which are carried out in the potential range of 0.01-3.0 V (vs. Li/Li^+) at a current density of 200 mA g^{-1}. As it can be seen in the initial discharge curves, the specific capacity of the hybrid electrodes gradually increase along with the increase of the Fe^{3+} concentration, and the α-Fe_2O_3@r-GO NFAs (2.0 mmol of $FeCl_3$ is added) electrode shows the maximum discharge capacity (ca. 2007.5 mAh g^{-1}). Nevertheless, for the α-Fe_2O_3@r-GO NFAs, the capacity declines rapidly from the 50th cycle and closes to only that of the α-Fe_2O_3@r-GO NRSAs after 300 cycles (ca. 1020 mAh g^{-1}). In contrast, the α-Fe_2O_3@r-GO NRAs shows the best cycling stability than other α-Fe_2O_3@r-GO hybrid samples (Fig. S8e),

so the following electrochemical performance measurements were focused on the α-Fe_2O_3@r-GO NRAs.

Fig. 7a illustrates the first five galvanostatic charge-discharge curves of the optimized α-Fe_2O_3@r-GO NRAs electrode at 200 mA g^{-1}. There are two obvious voltage plateaus (~1.60 and ~0.85 V) in the first discharge curve, which can be attributed to the lithium reactions with α-Fe_2O_3. The first potential plateau at ~1.60 V results from the formation of cubic α-$Li_2Fe_2O_3$, and the second potential plateau at ~0.85 V is due to the reduction of Fe^{3+} to Fe^0 and the formation of amorphous Li_2O. Furthermore, a more inclined discharge ramp in a potential range from 0.85 to 0.01 V stems from the contribution to the partial capacity of r-GO nanosheets, which is also well demonstrated in the initial r-GO electrode (Fig. S9a). The charge curve reveals a broad sloping plateau from 1.35 to 2.35 V checks with the reversible oxidation of Fe^0 to Fe^{3+}. The first discharge and charge capacities of the hybrid α-Fe_2O_3@r-GO NRAs electrode are ~1837.6 and ~1238.2 mA h g^{-1}, respectively, and then a negligible irreversible capacity loss from the first two cycles was found. The voltage-capacity trace of pure α-Fe_2O_3 NRs was also tested for comparison (Fig. 7b).

To observe the mechanism of the electrochemical reactions of lithium storage in α-Fe_2O_3@r-GO NRAs, the initial five cyclic voltammetry (CV) curves were carried out in the range of 0.01-3.0 V (vs. Li/Li^+) at a slow scan rate of 0.1 mV s^{-1}, as shown in Fig. 7c. The α-Fe_2O_3@r-GO NRAs electrode proceeds multiple steps electrochemical reactions, which can be expressed by the following equations [51-53]:

$$xLi \leftrightarrow xLi^+ + xe^- \quad (1)$$

$$\alpha - Fe_2O_3 + xLi^+ + xe^- \rightarrow \alpha - Li_xFe_2O_3 \quad (2)$$

$$\alpha - Li_xFe_2O_3 + (2-x)Li^+ + (2-x)e^- \rightarrow Li_2Fe_2O_3 \quad (3)$$

$$Li_2Fe_2O_3 + 4Li^+ + 4e^- \rightarrow 2Fe^0 + 3Li_2O \quad (4)$$

$$C_{r-GO} + yLi^+ + ye^- \leftrightarrow Li_yC_{r-GO} \quad (5)$$

According to previous reports, the broad cathodic peak at ~1.62 V tallies with the initial lithium insertion of α-Fe_2O_3 to $Li_xFe_2O_3$ (eqn (2)), and another very sharp signal cathodic peak at ~0.66 V corresponds to the reduction of Fe^{3+} to Fe^0 by Li and the formation of a solid electrolyte interphase (eqn (3)). There is a broad anodic peaks from 1.50 to 2.00 V during the delithiation process of the composite electrode, which are caused by the reversible multistep oxidation of Fe^0 to FeO and then to Fe_2O_3 (eqn (4)).[54] The strongest cathodic peak at ~0.66 V in the first cycle was shifted to ~0.73 V in the second cycle, owing to the polarization effect. More importantly, in the subsequent cycles, the CV curves

overlap very well, indicating that the hybrid α-Fe_2O_3@r-GO NRAs have excellent stability and high electrochemical reversibility. Meanwhile, for the pure r-GO and the as-prepared hybrid α-Fe_2O_3@r-GO electrode (Fig. S9b and Fig. 7c), the reduction peaks at 0.5 V reflect Li-ion intercalation in r-GO (eqn (5)).[55] Moreover, cyclic voltammograms were also investigated on the cells with α-Fe_2O_3 NRs for comparison (Fig. S9c).

To evaluate the cycle stability of the composite electrodes, the charge-discharge tests were carried out at room temperature rates up to 500 cycles with a current density of 0.2 C. Fig. 7d shows the extremely high cyclic stability of the α-Fe_2O_3@r-GO NRAs hybrid electrode. The capacity of the composite electrode shows a trivial decrease during the first 50 cycles followed by slow increase in the subsequent steps. A capacity of 1200 mAh g^{-1} is retained till 500 cycles at 0.2 C discharge/charge rates. Along with the increase of cycle numbers, the capacity enhancement can be mainly attributed to that more reacting sites of α-Fe_2O_3@r-GO NRAs were activated, participating in the Li-ion storage. Meanwhile, the hierarchical structures of the α-Fe_2O_3 nanorods/r-GO composite is still well maintained after 500 cycles, as shown in Fig. S10a and b. For comparison, control cells with pure r-GO and α-Fe_2O_3 NRs as electrodes were also tested. In order to further understand the rate capability of the α-Fe_2O_3@r-GO NRAs, the cycling response were performed at various current densities (Fig. 7e). All of the electrodes were first tested at the same current density of 0.1 C. It can be seen that an irreversible capacity losses are observed during the initial two cycles, which may be attributable to the decomposition of the electrolyte and/or solvent.[56, 57] Even so, the first discharge capacity of 2015.2 mA h g^{-1} for the α-Fe_2O_3@r-GO NRAs is higher than those of the α-Fe_2O_3 NRs (1605.8 mA h g^{-1}) and the r-GO (531.5 mA h g^{-1}). When the current density is gradually increased to 0.2 C, the specific capacity of the α-Fe_2O_3@r-GO NRAs is ~1180 mA h g^{-1}, which is slowly reduced to ~845 mA h g^{-1} at 0.8 C and ~775 mA h g^{-1} at 1.6 C, respectively. After 400 cycles, with the current being again returned back to 0.1 C, a specific capacity of ~1320 mA h g^{-1} can be recovered. Obviously, these capacities are also larger than those of the electrode made of α-Fe_2O_3 NRs and r-GO under the same conditions. Moreover, such a high specific capacity and rate performance is superior to those of previous Fe_2O_3 (or r-GO)-based and theirs hybrid composites electrodes (see detailed comparison in Table S1, Supporting Information). Herein, the improvement for our sample is believed to be resulted from the synergistic effect of between the Fe2O3 nanorods and r-GO nanosheets. The composites structure provides small ion/electron diffusion lengths in nanorod arrays, large enough opened spaces to buffer the volume expansion and fast electron transport pathway by highly conductive r-GO nanosheets.

In order to investigate the intrinsic electrochemical and kinetic mechanism of the hybrid electrode materials, electrochemical impedance spectroscopy (EIS) measurements were carried out. Fig.7f presents the Nyquist plots of the pure r-GO, α-Fe_2O_3 NRs, and α-Fe_2O_3@r-GO NRAs hybrid electrodes tested after the first cycles. Obviously, the Nyquist plots for α-Fe_2O_3@r-GO NRAs possess much smaller diameters of the semicircles in the high-medium frequency region than that of the pure α-Fe_2O_3 NRs, but much bigger than that of the pure r-GO, which indicates that α-Fe_2O_3@r-GO NRAs has smaller diameterindicate slower contact and charge-transfer resistances. The kinetic differences of the electrodes were further studied by the RC equivalent circuit model (inset of Fig. S9d). In the low-frequency area, the inclined line represents the Warburg (W) impedance, which is corresponding to the electrolyte diffusion in the porous electrode and proton diffusion in host materials. The α-Fe_2O_3@r-GO NRAs hybrid electrode reveals the higher slope value of the inclined line than the pure α-Fe_2O_3 NRs electrode, indicating a lower ion diffusion resistance, which can be accounted to the electrical conductivity improvement by the r-GO sheets. In the high and medium frequency area, the intercept to the real axis gives directly the bulk resistance of the electrochemical system (R_e), and the semicircle corresponds to a parallel combination of charge-transfer resistance (R_{ct}) and double-layer capacitance (CPE). Compared to the pure α-Fe_2O_3 NRs electrode, the α-Fe_2O_3@ r-GO NRAs composite electrode has a smaller R_e (1.48 Ω vs. 1.78 Ω), suggesting that the α-Fe_2O_3@r-GO NRAs hybrid electrode has a much better Li-ion diffusion and lower contact resistance. After 500 cycles, the R_{ct} slightly increases from 8.8 to 11.2 Ω, as shown in Fig. S9d, further demonstrating that long-time charge-discharge processes haven't damage the α-Fe_2O_3@r-GO NRAs hybrid electrode.

To further demonstrate the structure advantages of as-fabricated α-Fe_2O_3@r-GO NRAs, the sodium storage performances were also thoroughly examined. The CV curves of the α-Fe_2O_3@r-GO NRAs composite electrode of the first five cycles are displayed in Fig. 8a. According to the previous reports, the sodium insertion and extraction in Fe_2O_3 follows the reactions [58, 59]:

$$Fe_2O_3 + 6Na^+ + 6e^- \leftrightarrow 2Fe^0 + 3Na_2O \qquad (6)$$

During the first cycle, there are three reduction peaks located at 0.41, 0.83 and 1.39 V and three oxidation peaks located at 0.79, 1.45 and 1.84 V. The small peak at ~0.83 V and ~1.39 V are attributed to the Na^+ insertion into α-Fe_2O_3 and r-GO, respectively, forming α-$Na_xFe_2O_3$ and $Na_yC_{r\text{-}GO}$. The second obvious reduction peak at ~0.41 V can be assigned to a conversion of the α-Fe_2O_3 accompanied by the layer formation of solid electrolyte interface

(SEI).[60] The difference between the initial and the followed four cycles are mainly ascribed to the formation of SEI layer, leading to the irreversible capacity loss. In the following four cycles, a broad cathodic peak at ~0.67 V might be due to the conversion process of α-Fe_2O_3. The oxidation peaks at ~0.79 and ~1.45 V can be ascribed to a two-step oxidation of Fe^0 (i.e., $Fe^0 \rightarrow Fe^{+2}$ and $Fe^{+2} \rightarrow Fe^{+3}$, respectively).[26] Furthermore, the cyclic voltammograms of α-Fe_2O_3 NRs and pure r-GO were also measured and provided in Fig. 8b and Fig. S11a for comparison, respectively.

Fig. 8c presents the first five charge-discharge curves of α-Fe_2O_3@r-GO NRAs at 200 mA g^{-1}. The initial discharge and charge capacities of the α-Fe_2O_3@r-GO NRAs are 832.0 and 402.4 mAh g^{-1} with a Coulombic efficiency of 48.2 %. The capacity loss in the first cycle is mainly because of the formation of unstable SEI films by decomposition of electrolyte. However, the reversible capacity in the following cycles is very stable and maintains at ~350 mAh g^{-1}. For comparison, the voltage-capacity trace of α-Fe_2O_3 NRs and pure r-GO were also measured and provided in Fig. S11b and c. The rates performances of the composite electrodes are also examined by measuring the charge-discharge profiles under varied current densities. The second charge-discharge curves and the cycling capacities obtained for the α-Fe_2O_3@r-GO NRAs composite electrode at varied current densities from 0.1 C to 1.6 C (1 C ≈ 1000 mAg^{-1}) are presented in Fig. 8d and Fig. S12a, respectively. The α-Fe_2O_3@r-GO NRAs electrode exhibits a high reversible capacity of above 420 mA h g^{-1} at a current density of 0.1 C. Upon increasing the current density to 1.6 C, the specific capacity of the α-Fe_2O_3@r-GO NRAs composite electrode still maintains ~92 mA h g^{-1}. When the current rate returns to 0.1 C, the discharge capacity could still reach ~365 mA h g^{-1}, indicating the outstanding rates performance of the α-Fe_2O_3@r-GO NRAs composite electrode

The cycling performance of α-Fe_2O_3@r-GO NRAs, pure α-Fe_2O_3 NRs and bare r-GO sheets at a constant current density of 200 mA g^{-1} for the first 300 cycles were shown in Fig. 8e. The reversible specific capacity of original r-GO nanosheets decreased from 56.8 mA h g^{-1} to 37.8 mA h g^{-1} during the 300 cycles. Although the pure α-Fe_2O_3 NRs shown high reversible capacities in the first cycle with a good Coulomb efficiency (~532 mA h g^{-1}), the discharge capacity of the anode material rapidly declined to ~118 mA h g^{-1} after 50 cycles, then the specific capacity was still maintained at ~90 mA h g^{-1} in the following cycle, which is only about 6% of the initial capacity. In contrast, the α-Fe_2O_3@r-GO NRAs electrode shows a good discharge capacity of 403 mAh g^{-1} in the second cycle. During the initial 10 cycles, the capacity decreased slowly to around 338 mAh g^{-1}, and then maintained at ~332 mAh g^{-1} up to the 300^{th} cycle. Moreover, even at 1.6 C (Fig. S12b), the capacity remained

close to 65.6 % after 800 cycles for the α-Fe_2O_3@r-GO NRAs, demonstrating the excellent cycling stability of the composite electrode. The performance is superior to most of the previous reported Fe_2O_3 or Fe_2O_3/graphene hybrid composites electrodes, for instance, nanostructured Fe_2O_3[61], and nanopore-structured γ-Fe_2O_3 film[60], α-Fe_2O_3/rGO nanocomposites[62], and Fe_2O_3@GNS composite[59] (listed in Table S2, Supporting Information).

The above obtained superior electrochemical performance of the α-Fe_2O_3@r-GO NRAs hybrid electrode might reasonably be attributed to the unique 3D composite array structures and directly growth on r-GO conductive substrate (Fig. 8f). First, the porous structures of α-Fe_2O_3 nanorod arrays and the open space between adjacent nanorods are beneficial to electrolyte infiltration and accommodate the volume change during the Na^+ uptake and release process. Second, the in-situ fabricated α-Fe_2O_3 nanorods on r-GO sheets achieve good electronic contact, which promotes the electrons flowing between the r-GO conductive layer and α-Fe_2O_3 nanorods. Besides, the r-GO substrate with high electrical conductivity can enhance the reaction kinetics towards fast sodium insertion/extraction.

4. Conclusions

In summary, we have successfully fabricated α-Fe_2O_3@r-GO NRAs composites with 1D α-Fe_2O_3 nanorod arrays assembling on double-faces of 2D r-GO nanosheets using a seed-assisted hydrothermal growth method. The as-fabricated α-Fe_2O_3@r-GO NRAs were further tested as anodes for both LIBs and SIBs, which exhibited superior electrochemical storage performance in terms of capacity, cycling stability and rates capability. The improved performances can be attributed to the unique hybrid structure design, which provides fast electron transport and short diffusion paths of the Li-ion or Na-ion and accommodate the volume variation of the composite electrode during the charging-discharging process. This facile and scalable synthesis route opens up new chances to design of 2D/1D graphene-based hybrids composites for superior anodes in Li-ion and Na-ion batteries.

Acknowledgements

This work is financially supported by the 973 Program (Grant no. 2013CB632701), the National Natural Science Foundation of China (Grant no. 51202163). H. Y. Yang acknowledges the financial support of SUTD-MIT International Design Center funding (IDG21400109).

References

1. J. L. Xie, C. X. Guo and C. M. Li, *Energy Environ. Sci.*, 2014, **7**, 2559-2579.
2. M. Y. Yan, F. C. Wang, C. H. Han, X. Y. Ma, X. Xu, Q. Y. An, L. Xu, C. J. Niu, Y. L. Zhao, X. C. Tian, P. Hu, H. G. Wu and L. Q. Mai, *J. Am. Chem. Soc.*, 2013, **135**, 18176-18182.
3. D. L. Chao, C. R. Zhu, X. H. Xia, J. L. Liu, X. Zhang, J. Wang, P. Liang, J. Y. Lin, H. Zhang, Z. X. Shen and H. J. Fan, *Nano Lett.*, 2015, **15**, 565-573.
4. B. Zhao, R. Ran, M. L. Liu and Z. P. Shao, *Materials Science and Engineering R*, 2015, **98**, 1-71.
5. M. V. Reddy, G. V. S. Rao and B. V. R. Chowdari, *Chem. Rev.*, 2013, **113**, 5364-5457.
6. D. Z. Kong, W. N. Ren, Y. S. Luo, Y. P. Yang and C. W. Cheng, *J. Mater. Chem. A*, 2014, **2**, 20221-20230.
7. Z. Wang, L. Zhou and X. W. Lou, *Adv. Mater.*, 2012, **24**, 1903-1911.
8. Y. Wang, B. Chen, D. H. Seo, Z. J. Han, J. I. Wong, K. K. Ostrikov, H. Zhang, H. Y. Yang, *NPG Asia Mater.*, 2016, 8, e268.
9. M. D. Slater, D. Kim, E. Lee and C. S. Johnson, *Adv. Funct. Mater.*, 2013, **23**, 947-958.
10. Y. H. Liu, Y. H. Xu, Y. J. Zhu, J. N. Culver, C. A. Lundgren, K. Xu and C. S. Wang, *ACS Nano*, 2013, **7**, 3627-3634.
11. S. Y. Hong, Y. Kim, Y. Park, A. Choi, N. S. Choi, K. T. Lee, *Energy Environ. Sci.*, 2013, **6**, 2067-2081.
12. Y. X. Wang, Y. G. Lim, M. S. Park, S. L. Chou, J. H. Kim, H. K. Liu, S. X. Dou and Y. J. Kim, *J. Mater. Chem. A*, 2014, **2**, 529-534.
13. Z. J. Zhang, Y. X. Wang, S. L. Chou, H. J. Li, H. K. Liu and J. Z. Wang, *J. Power Sources*, 2015, **280**, 107-113.
14. N. Yabuuchi, K. Kubota, M. Dahbi and S. Komaba, *Chem. Rev.*, 2014, **114**, 11636-11682.
15. Y. J Fang, L. F. Xiao, J. F. Qian, X. P. Ai, H. X. Yang and Y. L. Cao, *Nano Lett.*, 2014, **14**, 3539-3543.
16. S. Y. Hong, Y. Kim, Y. Park, A. Choi, N. Choic and K. T. Lee, *Energy Environ. Sci.*, 2013, **6**, 2067-2081.
17. J. X. Guo, H. F. Zhu, Y. F. Sun and X. Zhang, *J. Mater. Chem. A*, 2015, 3, 19384-19392.
18. D. Z. Kong, J. S. Luo, Y. L. Wang, W. N. Ren, T. Yu, Y. S. Luo, Y. P. Yang, C. W. Cheng, *Adv. Funct. Mater.*, 2014, **24**, 3815-3826.

19. B. Wang, H. B. Wu, L. Zhang and X. W. Lou, *Angew. Chem., Int. Ed.*, 2013, **52**, 4165-4168.
20. X. Zhang, H. X. Chen, Y. P. Xie and J. X. Guo, *J. Mater. Chem. A*, 2014, **2**, 3912-3918.
21. N. Spinner, L. C. Zhang and W. E. Mustain, *J. Mater. Chem. A*, 2014, **2**, 1627-1630.
22. L. Zhang, H. B. Wu and X. W. Lou, *Adv. Energy Mater.,* 2014, **4**, 1300958.
23. Y. S. Luo, J. S. Luo, J. Jiang, W. W. Zhou, H. P. Yang, X. Y. Qi, H. Zhang, H. J. Fan, D. Y. W. Yu, C. M. Li and T. Yu, *Energy Environ. Sci.*, 2012, **5**, 6559-6566.
24. L. S. Xiao, M. Schroeder, S. Kluge, A. Balducci, U. Hagemann, C. Schulz and H. Wiggers, *J. Mater. Chem. A*, 2015, **3**, 11566-11574.
25. B. Zhao, Y. Zheng, F. Ye, X. Deng, X. M. Xu, M. L. Liu and Z. P. Shao, *ACS Appl. Mater. Interfaces*, 2015, **7**, 14446-14455.
26. J. S. Luo, X. H. Xia, Y. S. Luo, C. Guan, J. L. Liu, X. Y. Qi, C. F. Ng, T. Yu, H. Zhang, and H. J. Fan, *Adv. Energy Mater.*, 2013, **3**, 737-743.
27. J. H. Wang, M. X. Gao, H. G. Pan, Y. F. Liu, Z. Zhang, J. X. Li, Q. M. Su, G. H. Du, M. Zhu, L. Z. Ouyang, C. X. Shang and Z. X. Guo, *J. Mater. Chem. A*, 2015, **3**, 14178-14187.
28. N. Yan, X. H. Zhou, Y. Li, F. Wang, H. Zhong, H. Wang and Q. W. Chen, *Sci. Rep.*, 2013, **3**, 3392.
29. A. Varzi, C. Taubert, M. Wohlfahrt-Mehrens, M. Kreis and W. Schutz, *J. Power Sources*, 2011, **196**, 3303-3309.
30. Y. Q. Zou, J. Kan and Y. Wang, *J. Phys. Chem. C*, 2011, **115**, 20747-20753.
31. G. X. Gao, H. B. Wu, B. T. Dong, S. J. Ding and X. W. Lou, *Adv. Sci.*, 2015, **2**, 1400014.
32. M. H. Chen, J. L. Liu, D. L. Chao, J. Wang, J. H. Yin, J. Y. Li, H. J. Fan and Z. X. Shen, *Nano Energy*, 2014, **9**, 364-372.
33. Z. Y. Wang and C. J. Liu, *Nano Energy*, 2015, **11**, 277-293.
34. X. Wang, W. Tian, D. Q. Liu, C. Y. Zhi, Y. Bando, D. Golberg, *Nano Energy*, 2013, **2**, 257-267.
35. H. M. Zhang, C. L. Zhu, Y. J. Chen and H. Gao, *ChemPhysChem*, 2014, **15**, 2261-2266.
36. L. Wang, Y. J. Ye, X. P. Lu, Z. B. Wen, Z. Li, H. Q. Hou and Y. H. Song, *Sci. Rep.*, 2013, **3**, 3568.
37. L. F. He, R. G. Ma, N. Du, J. G. Ren, T. L. Wong, Y. Y. Li and S. T. Lee, *J. Mater. Chem.*, 2012, **22**, 19061-19066.
38. G. X. Gao, S. Y. Lu, Y. Xiang, B. T. Dong, W. Yan and S. J. Ding, *Dalton Trans.*, 2015, **44**, 18737-18742.

39. W. S. Hummers and R. E. Offeman, *J. Am. Chem. Soc.*, 1958, **80**, 1339-1340.
40. S. K. Liu, Z. X. Chen, K. Xie, Y. J. Li, J. Xu and C. M. Zheng, *J. Mater. Chem. A*, 2014, **2**, 13942-13948.
41. A. A. Tahir, K. G. U. Wijayantha, S. Saremi-Yarahmadi, M. Mazhar and V. McKee, *Chem. Mater.*, 2009, **21**, 3763-3772.
42. G. K. Pradhan and K. M. Parida, *ACS Appl. Mater. Interfaces*, 2011, **3**, 317-323.
43. S. L. Bai, K. W. Zhang, J. H. Sun, R. X. Luo, D. Q. Li and A. F. Chen, *CrystEngComm*, 2014, **16**, 3289-3295.
44. X. L. Wang, J. Mujtaba, F. Fang, M. Ahmad, H. Arandiyan, H. P. Yang, G. X. Sun and H. Y. Sun, *RSC Adv.*, 2015, **5**, 91574-91580.
45. Y. L. Dong, X. F. Zhang, X. L. Cheng, Y. M. Xu, S. Gao, H. Zhao and L. H. Huo, *RSC Adv.*, 2014, **4**, 57493-57500.
46. B. Li, H. Cao, J. Shao, G. Li, M. Qu and G. Yin, *Inorg. Chem.*, 2011, **50**, 1628-1632.
47. J. X. Guo, L. Chen, G. J. Wang, X. Zhang and F. F. Li, *J Power Sources*, 2014, **246**, 862-867.
48. R. H. Wang, C. H. Xu, J. Sun and L. Gao, *Sci. Rep.*, 2014, **4**, 7171.
49. Z. L. Liu, S. W. Tay and X. Li, *Chem. Commun.*, 2011, **47**, 12473-12475.
50. Y. L. Ren, C. L. Zhu, S. Zhang, C. Y. Li, Y. J. Chen, P. Gao, P. P. Yang and Q. Y. Ouyang, *Nanoscale*, 2013, **5**, 12296-12303.
51. S. P. Zhu, M. Chen, W. J. Ren, J. R. Yang, S. S. Qu, Z. C. Li and G. W. Diao, *New J. Chem.*, 2015, **39**, 7923-7931.
52. S. Chen, Y. L. Xin, Y. Y. Zhou, F. Zhang, Y. R. Ma, H. H. Zhou and L. M. Qi, *J. Mater. Chem. A*, 2015, **3**, 13377-13383.
53. X. Y. Xue, C. H. Ma, C. X. Cui and L. L. Xing, *Solid State Sci.*, 2011, **13**, 1526-1530.
54. S. Saadat, J. Zhu, D. H. Sim, H. H. Hng, R. Yazami and Q. Y. Yan, *J. Mater. Chem. A*, 2013, **1**, 8672-8678.
55. D. Z. Kong, C. W. Cheng, Y. Wang, J. I. Wong, Y. P. Yang and H. Y. Yang, *J. Mater. Chem. A*, 2015, **3**, 16150-16161.
56. A. M. Haregewoin, A. S. Wotango and B. Hwang, *Energy Environ. Sci.*, 2016, **9**, 1955-1988.
57. J. B. Cheng, Y. Lu, K. W. Qiu, H. L. Yan, J. Y. Xu, L. Han, X. M. Liu, J. S. Luo, J. Kim and Y. S. Luo, *Sci. Rep.*, 2015, **5**, 12099.
58. N. Zhang, X. P. Han, Y. C. Liu, X. F. Hu, Q. Zhao and J. Chen, *Adv. Energy Mater.*, 2015, **5**, 1401123.

59. Z. L. Jian, B. Zhao, P. Liu, F. J. Li, M. B. Zheng, M. W. Chen, Y. Shi and H. S. Zhou, *Chem. Commun.*, 2014, **50**, 1215-1217.

60. M. Valvo, F. Lindgren, U. Lafont, F. Björefors and K. Edström, *J. Power Sources*, 2014, **245**, 967-978.

61. S. B. Wang, W. Wang, P. Zhan and S. Q. Jiao, *ChemElectroChem,* 2014, **1**, 1636-1639.

62. Z. J. Zhang, Y. X. Wang, S. L. Chou, H. J. Li, H. K. Liu and J. Z. Wang, *J. Power Sources,* 2015, **280**, 107-113.

Figure captions

Fig. 1 Schematic illustration of the fabrication process for α-Fe_2O_3 nanorod arrays on reduced graphene oxide nanosheets.

Fig. 2 FESEM images of (a) α-Fe_2O_3 NRs, (b) r-GO sheets, (c, d) Fe-precursor NPs seed-assisted on r-GO sheets and (e, f) *α*-Fe_2O_3@r-GO NRAs. Inset in (a), (b) and (d) are the HRSEM images for α-Fe_2O_3 NRs, r-GO sheets, Fe-precursor NPs seed-assisted on r-GO sheets and *α*-Fe_2O_3@r-GO NRAs, respectively.

Fig. 3 TEM images of (a, b) α-Fe_2O_3 NRs, (c, d) r-GO nanosheets and (e, f) α-Fe_2O_3@r-GO NRAs. The insets show the corresponding SAED pattern.

Fig. 4 XRD patterns (a) and Raman spectra (b) of *α*-Fe_2O_3@r-GO NRAs, α-Fe_2O_3 NRs and r-GO nanosheets.

Fig. 5 (a) SEM image and corresponding EDS elemental mappings of Fe, O, C, and Cu for the α-Fe_2O_3@r-GO NRAs; (b) The EDS microanalysis and the corresponding elemental contents on selected areas of the α-Fe_2O_3@r-GO NRAs, α-Fe_2O_3 NRs and r-GO sheets; (c) TGA curves of the α-Fe_2O_3@r-GO NRAs, α-Fe_2O_3 NRs and r-GO sheets in oxygen atmosphere; (d) Nitrogen adsorption-desorption isotherm and BJH adsorption pore-size distribution for the obtained α-Fe_2O_3@r-GO NRAs.

Fig. 6 SEM images of *α*-Fe_2O_3@r-GO hybrids prepared with various amounts of $FeCl_3$ during the second hydrothermal process: (a) 0; (b) 0.4 mmol; (c) 0.8 mmol; (d) 1.2 mmol; (e) 1.6 mmol; (f) 2.0 mmol (marked as *α*-Fe_2O_3@r-GO NRAs, *α*-Fe_2O_3@r-GO NSRAs, *α*-Fe_2O_3@r-GO NRSAs, *α*-Fe_2O_3@r-GO NRAs, and *α*-Fe_2O_3@r-GO NFAs, respectively). (g) Proposed mechanism for the corresponding on the morphology construction.

Fig. 7 Galvanostatic discharge/charge profiles of the *α*-Fe_2O_3@r-GO NRAs anode (a) and the pure *α*-Fe_2O_3 NRs anode (b) at a constant current density of 200 mA g^{-1}. (c) CV curve of a *α*-Fe_2O_3@r-GO NRAs anode at 0.1 mV s^{-1} scanning rate. (d) Cycling performance of the anodes at a constant current density of 200 mA g^{-1}. (e) Reversible capacity vs. current density (rate capability) for different anodes. (f) Equivalent circuit and electrochemical impedance spectra after the 1st cycle.

Fig. 8 CV curves of the *α*-Fe_2O_3@r-GO NRAs anode (a) and the pure *α*-Fe_2O_3 NRs anode (b) at 0.1 mV s^{-1} scanning rate. (c) Galvanostatic discharge/charge profiles of a *α*-Fe_2O_3@r-GO NRAs anode at a constant current density of 200 mA g^{-1}. (d) Discharge/charge cures of the *α*-Fe_2O_3@r-GO NRAs anode at different rates. (e) Cycling performance of the anodes at a constant current density of 200 mA g^{-1}. (f) Schematic representation of rechargeable Na-ion battery based on *α*-Fe_2O_3@r-GO NRAs.

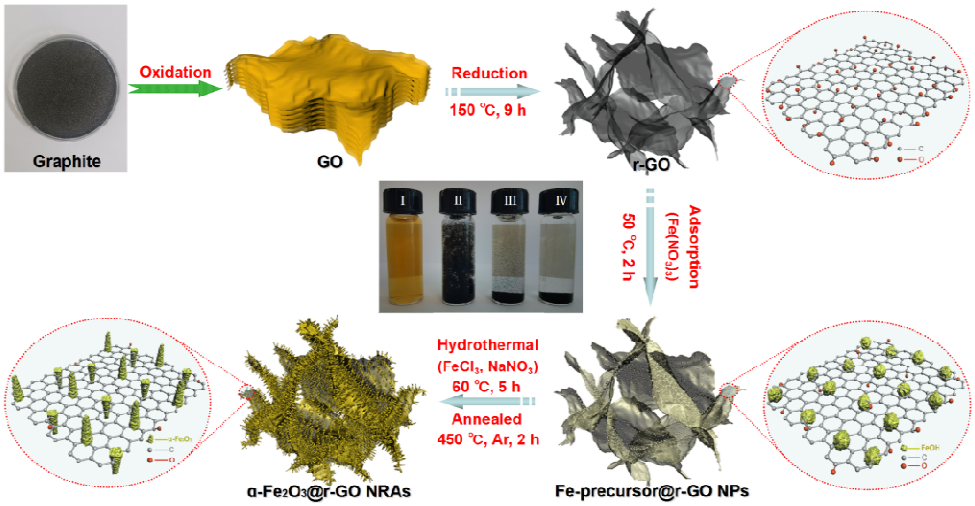

Fig. 1 Schematic illustration of the fabrication process for α-Fe_2O_3 nanorod arrays on reduced graphene oxide nanosheets.

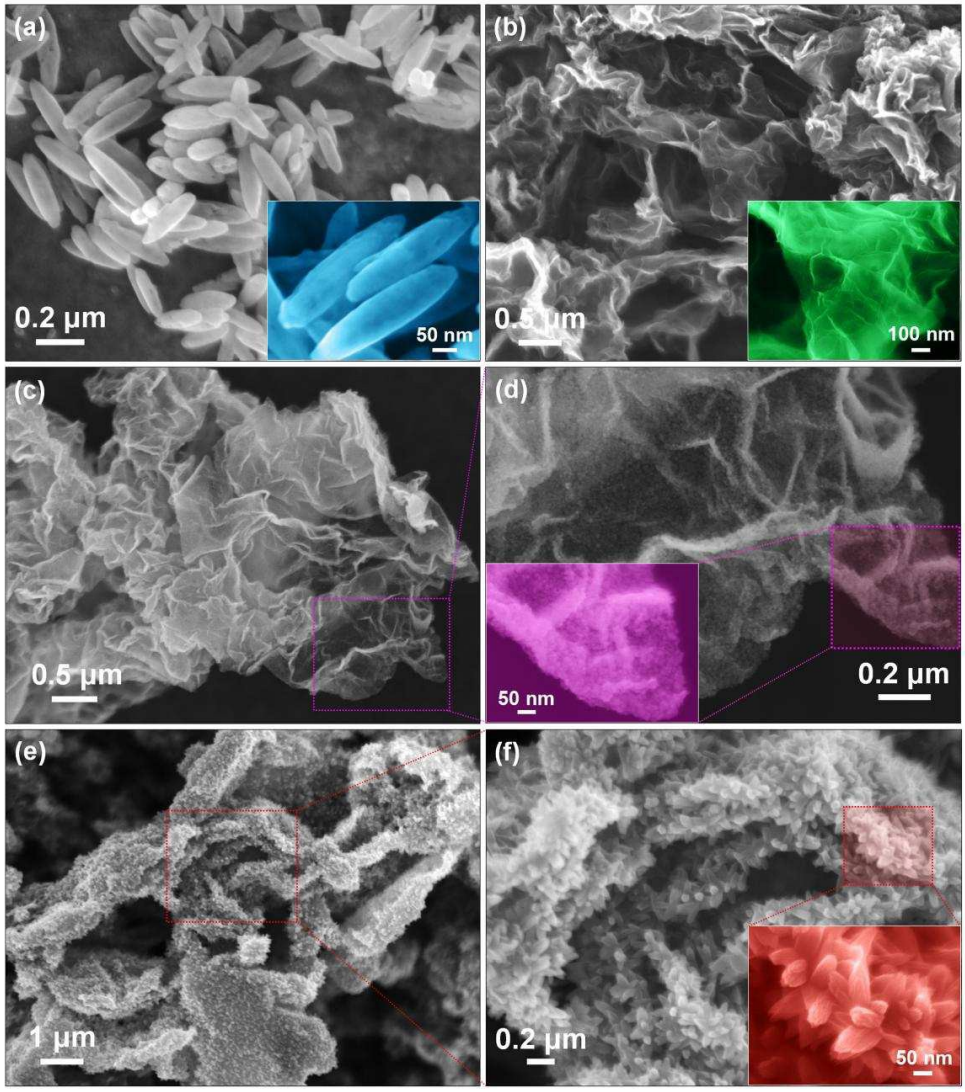

Fig. 2 FESEM images of (a) α-Fe_2O_3 NRs, (b) r-GO sheets, (c, d) Fe-precursor NPs seed-assisted on r-GO sheets and (e, f) *α*-Fe_2O_3@r-GO NRAs. Inset in (a), (b) and (d) are the HRSEM images for α-Fe_2O_3 NRs, r-GO sheets, Fe-precursor NPs seed-assisted on r-GO sheets and *α*-Fe_2O_3@r-GO NRAs, respectively.

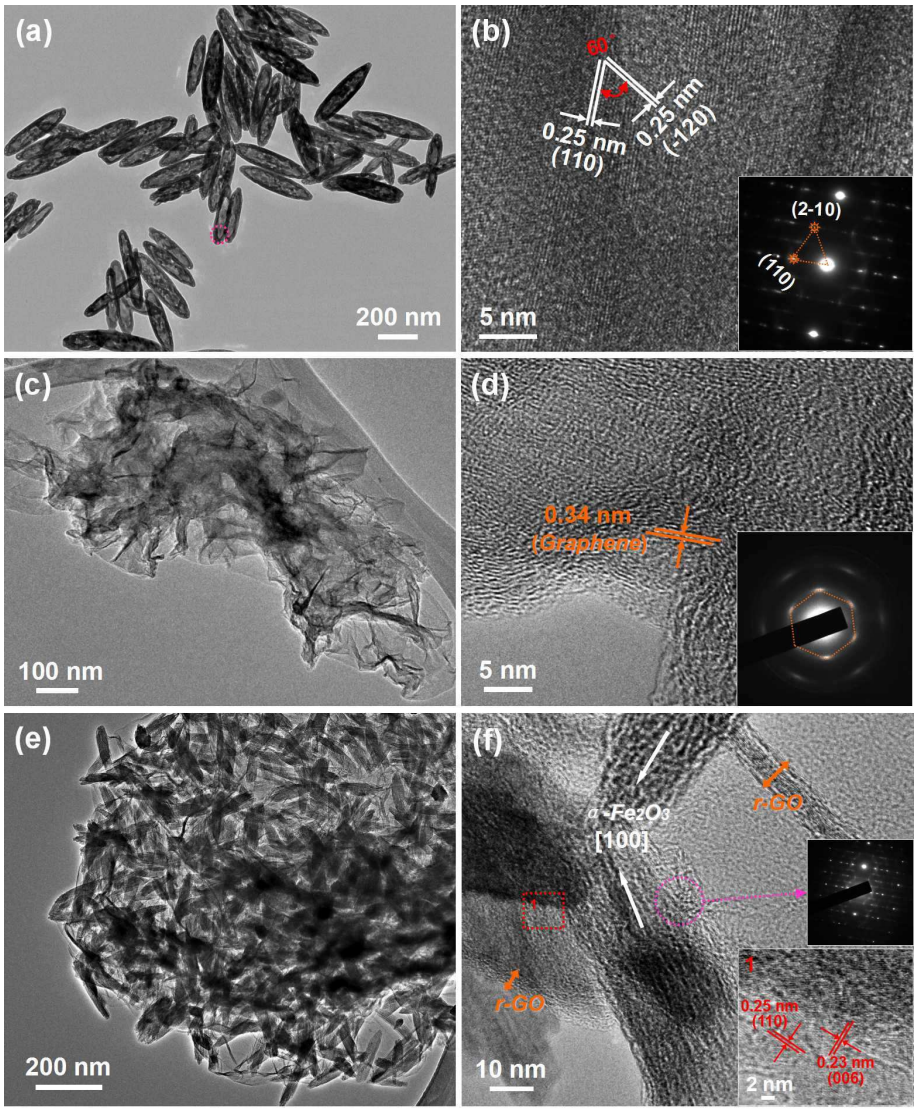

Fig. 3 TEM images of (a, b) α-Fe_2O_3 NRs, (c, d) r-GO nanosheets and (e, f) α-Fe_2O_3@r-GO NRAs. The insets show the corresponding SAED pattern.

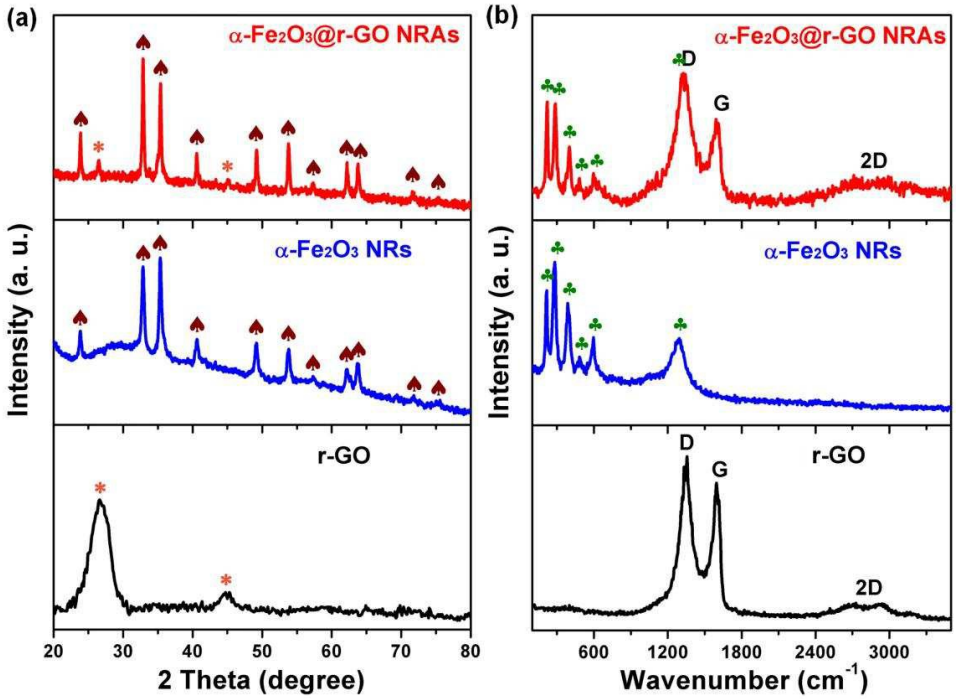

Fig. 4 XRD patterns (a) and Raman spectra (b) of α-Fe_2O_3@r-GO NRAs, α-Fe_2O_3 NRs and r-GO nanosheets.

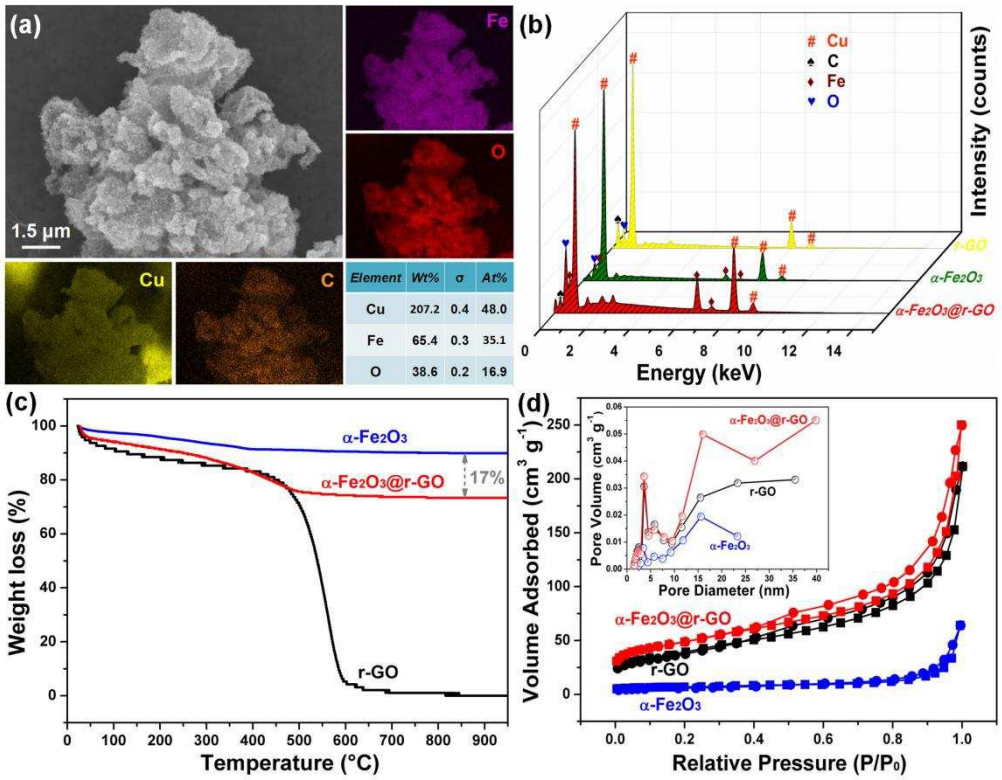

Fig. 5 (a) SEM image and corresponding EDS elemental mappings of Fe, O, C, and Cu for the α-Fe_2O_3@r-GO NRAs; (b) The EDS microanalysis and the corresponding elemental contents on selected areas of the α-Fe_2O_3@r-GO NRAs, α-Fe_2O_3 NRs and r-GO sheets; (c) TGA curves of the α-Fe_2O_3@r-GO NRAs, α-Fe_2O_3 NRs and r-GO sheets in oxygen atmosphere; (d) Nitrogen adsorption-desorption isotherm and BJH adsorption pore-size distribution for the obtained α-Fe_2O_3@r-GO NRAs.

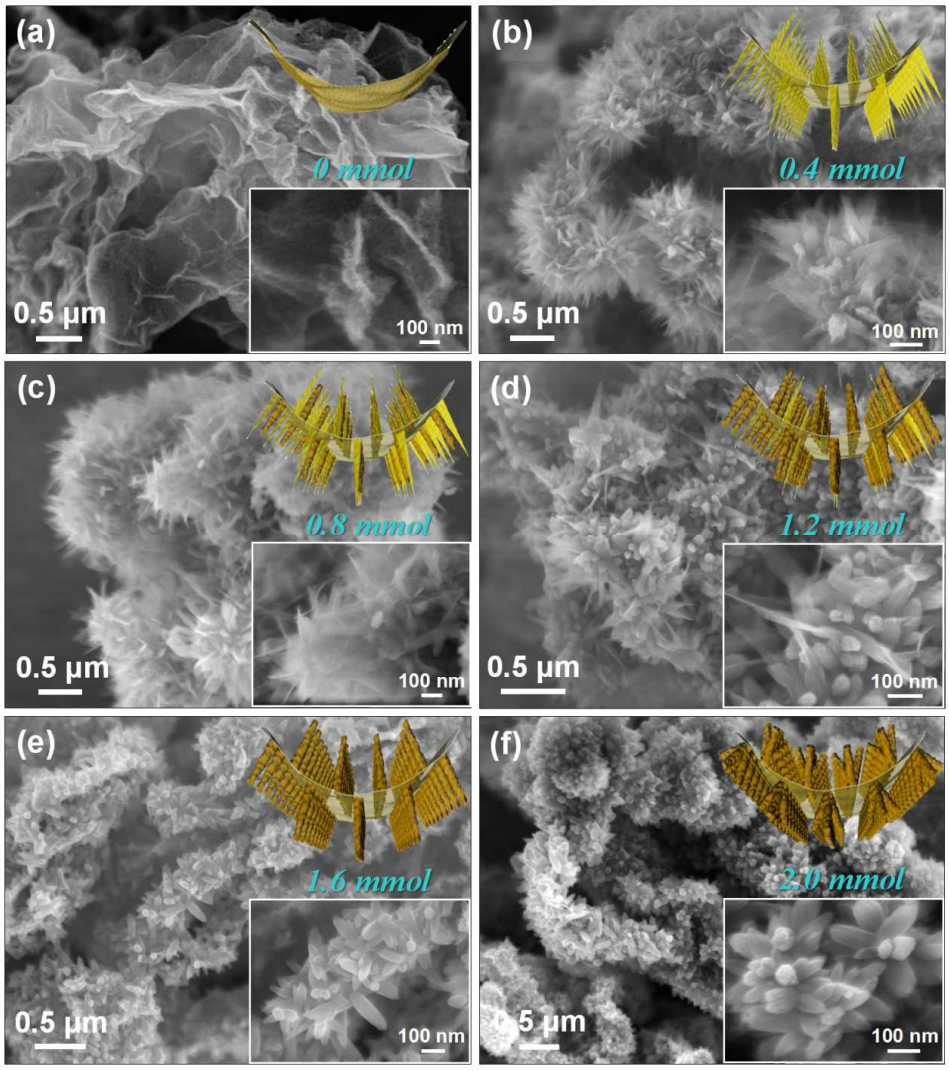

Fig. 6 SEM images of α-Fe_2O_3@r-GO hybrids prepared with various amounts of $FeCl_3$ during the second hydrothermal process: (a) 0; (b) 0.4 mmol; (c) 0.8 mmol; (d) 1.2 mmol; (e) 1.6 mmol; (f) 2.0 mmol (marked as α-Fe_2O_3@r-GO NSAs, α-Fe_2O_3@r-GO NSRAs, α-Fe_2O_3@r-GO NRSAs, α-Fe_2O_3@r-GO NRAs, and α-Fe_2O_3@r-GO NFAs, respectively).

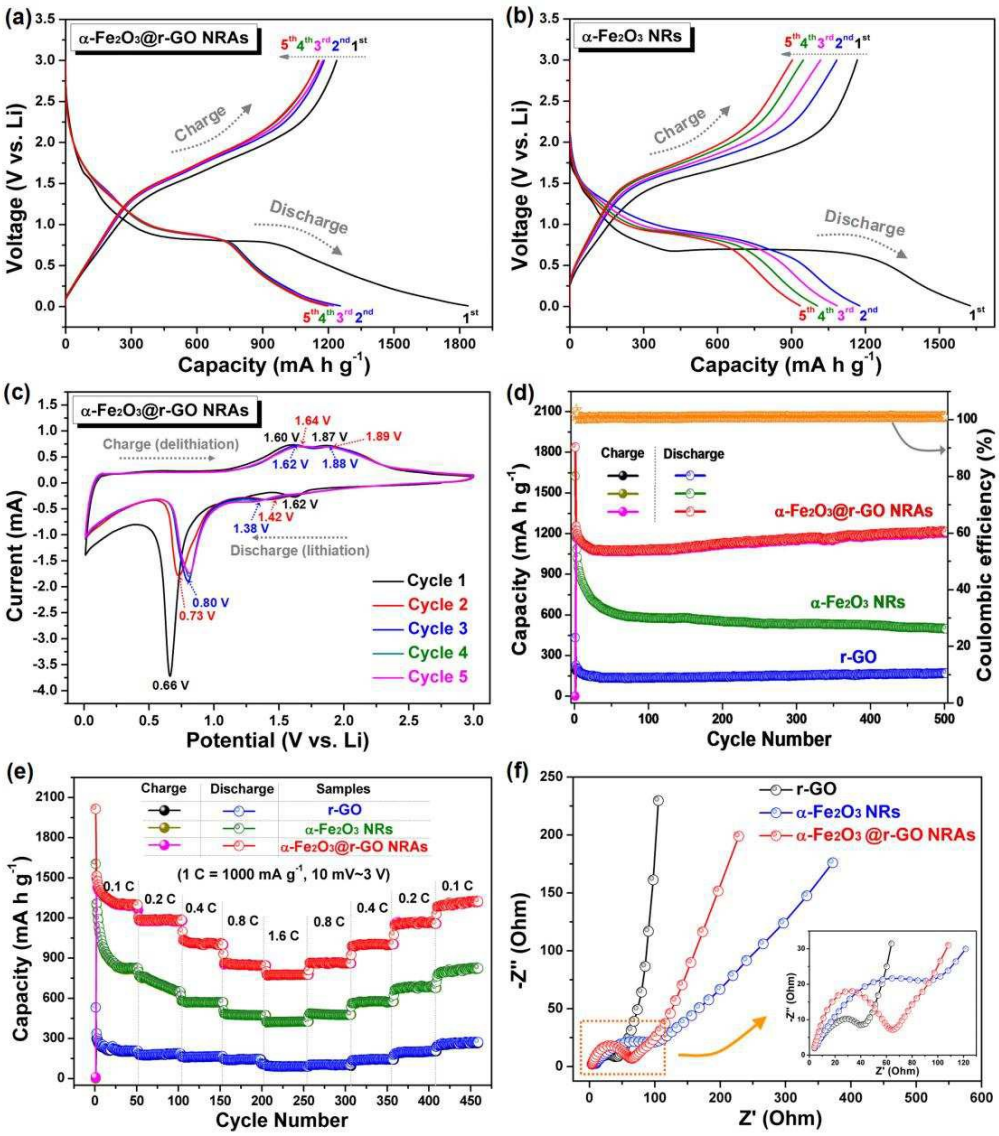

Fig. 7 Galvanostatic discharge/charge profiles of the α-Fe_2O_3@r-GO NRAs anode (a) and the pure α-Fe_2O_3 NRs anode (b) at a constant current density of 200 mA g^{-1}. (c) CV curve of a α-Fe_2O_3@r-GO NRAs anode at 0.1 mV s^{-1} scanning rate. (d) Cycling performance of the anodes at a constant current density of 200 mA g^{-1}. (e) Reversible capacity vs. current density (rate capability) for different anodes. (f) Equivalent circuit and electrochemical impedance spectra after the 1st cycle.

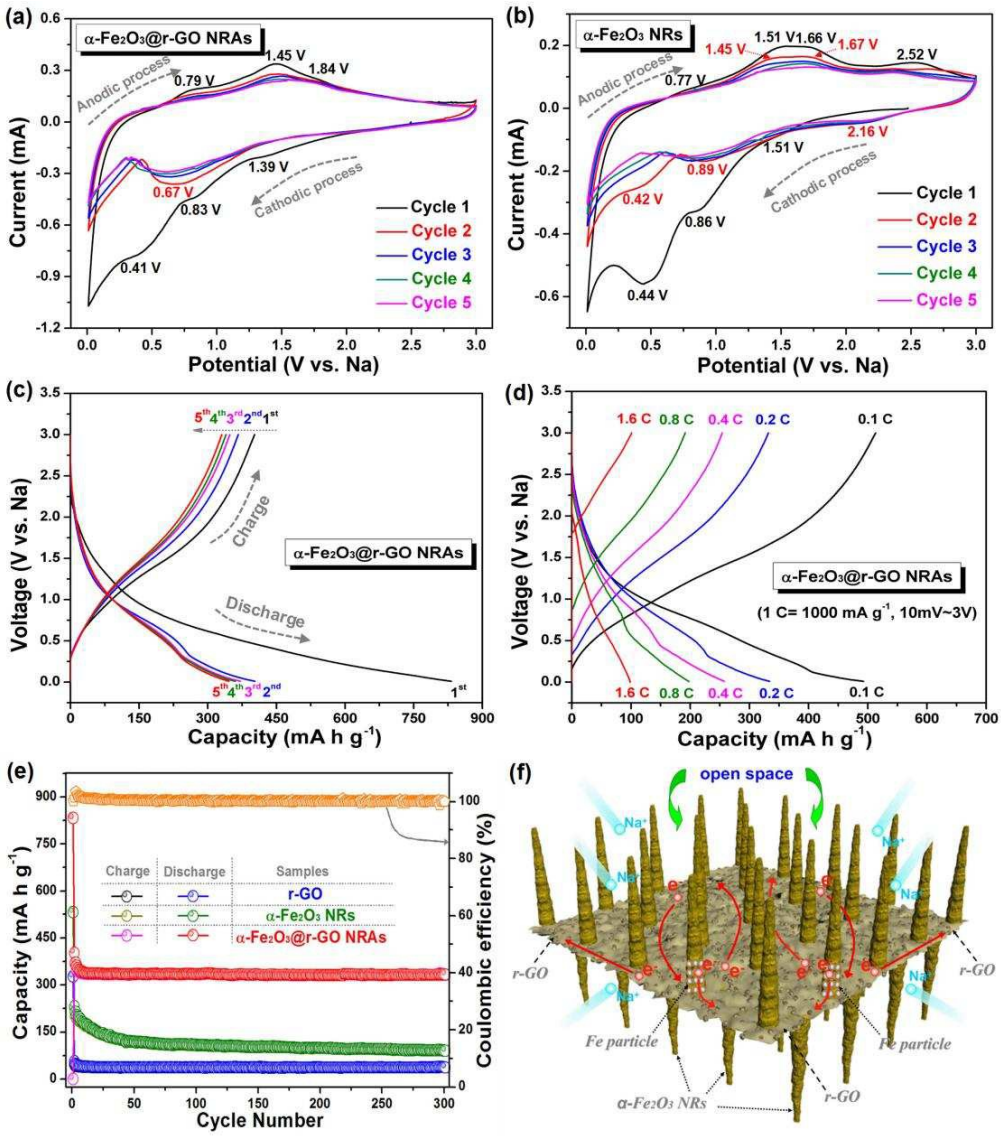

Fig. 8 CV curves of the α-Fe_2O_3@r-GO NRAs anode (a) and the pure α-Fe_2O_3 NRs anode (b) at 0.1 mV s^{-1} scanning rate. (c) Galvanostatic discharge/charge profiles of a α-Fe_2O_3@r-GO NRAs anode at a constant current density of 200 mA g^{-1}. (d) Discharge/charge cures of the α-Fe_2O_3@r-GO NRAs anode at different rates. (e) Cycling performance of the anodes at a constant current density of 200 mA g^{-1}. (f) Schematic representation of rechargeable Na-ion battery based on α-Fe_2O_3@r-GO NRAs.

The table of contents entry

Keyword: α-Fe_2O_3 nanorods, reduced graphene oxide, anode material, lithium ion battery, sodium ion battery.

Dezhi Kong, Chuanwei Cheng,* Ye Wang, Bo Liu, Zhixiang Huang, and Hui Ying Yang*

Seed-assisted growth of α-Fe_2O_3 nanorod arrays on reduced graphene oxide: A superior anode for high-performance Li-ion and Na-ion batteries

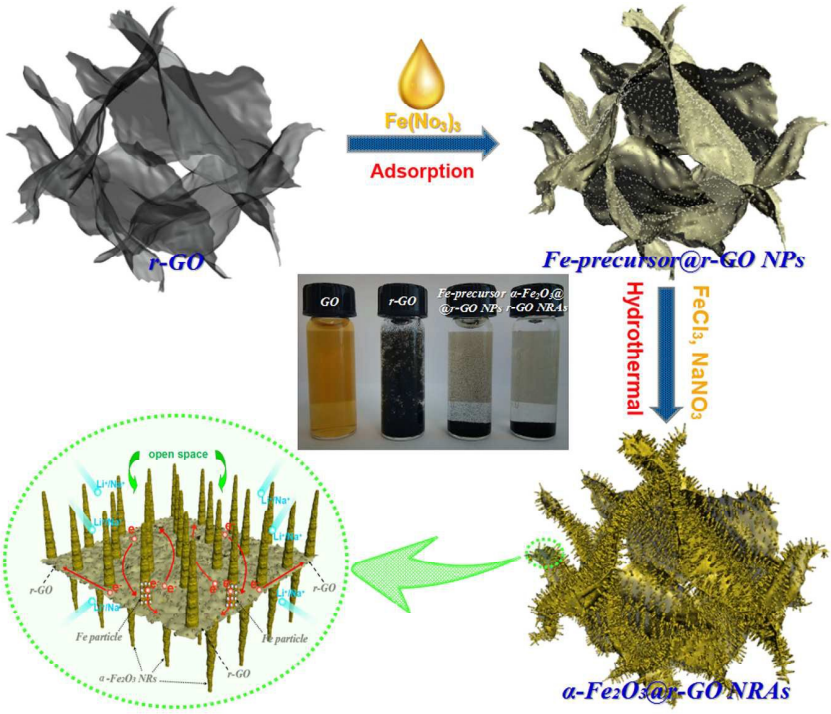

An α-Fe_2O_3 nanorods/reduced graphene oxide nanosheets composites (denoted as α-Fe_2O_3@r-GO NRAs) are fabricated by a facile and scalable seeds-assisted hydrothermal growth route and further investigated as superior anodes for both lithium-ion and sodium-ion batteries (LIBs and SIBs) with high capacity and long-cycling life.